*Geophys. J. Int.* (2004) **157,** 293–304 doi: 10.1111/j.1365-246X.2004.02194.x

# Multiple resolution surface wave tomography: the Mediterranean basin

L. Boschi,[1,2]* G. Ekström[3] and B. Kustowski[3]

[1] *Dipartimento di Scienze Fisiche, Università Federico II, Napoli, Italy*
[2] *Institute of Geophysics, ETH Hönggerberg, Zürich, Switzerland*
[3] *Department of Earth and Planetary Sciences, Harvard University, Cambridge, MA, USA*

Accepted 2003 November 14. Received 2003 October 20; in original form 2003 January 31

## SUMMARY

From a large set of fundamental-mode surface wave phase velocity observations, we map the transversely isotropic lateral heterogeneities in the upper-mantle shear velocity structure. We design a multiple resolution inversion procedure, which allows us to parametrize any selected region more finely than the rest of the globe. We choose, as a high-resolution region, the upper mantle underlying the Mediterranean basin. We formulate the inverse problem as in a previous paper by Boschi & Ekström, calculating regional JWKB (Jeffreys–Wentzel–Kramers–Brillouin) surface wave sensitivity kernels for each pixel of a $2^\circ \times 2^\circ$ starting model, including the high-resolution global crustal map Crust 2.0. We find that the available surface wave data can resolve the most important geophysical features of the region of interest, providing a reliable image of intermediate spatial wavelength.

**Key words:** JWKB, Mediterranean basin, seismic tomography, surface waves.



## 1 INTRODUCTION

The Mediterranean basin is a geodynamically complex area, governed by the slow collision between Africa and Eurasia. The boundary between the two plates is not entirely well defined: although there is clear geodetic and seismic evidence of northward subduction under the Hellenic and Calabrian arcs, diffuse seismicity around the Adriatic sea and western Mediterranean requires a more complex description of plate interaction (e.g. de Jonge *et al.* 1994; Wortel & Spakman 2000; Faccenna *et al.* 2001). Tomographic studies of the region naturally play an important role in this context.

Our current knowledge of the upper mantle underlying the Mediterranean basin is mostly derived, through seismic tomography, from observations of teleseismic and regional body wave travel times (e.g. Spakman *et al.* 1993; Piromallo & Morelli 1997; Bijwaard 1999; Piromallo & Morelli 2003).

Teleseismic body waves, covering epicentral distances of *ca* 25° and more, propagate almost vertically within most of the upper mantle, and reach their bottoming point only in the lower mantle. For this reason, a set of teleseismic body wave measurements is optimal to map the lower mantle lateral structure, but can achieve only a limited resolution of the upper mantle: at shallow depths it only illuminates a, more or less, narrow cone below each seismic source and receiver.

Regional body waves travel entirely within the upper mantle, and are in principle a better means for its imaging. They are, on the other hand, more difficult to observe and interpret; the very strong radial and lateral heterogeneities that characterize the Earth's crust and shallowest upper mantle can give rise to shadow zones, triplications, and significant deviations of ray paths from their 1-D reference shape (in large-scale body wave tomography, ray paths are calculated in a 1-D reference model and it is assumed that they are only negligibly affected by lateral anomalies). All this naturally limits the resolution that these observations can provide (e.g. Shearer 1999).

It is understood that the latter difficulties, since they concern the formulation of the forward problem, cannot be evidenced by the usual checkerboard or resolution tests, which only measure the adequacy of the distribution of sources and receivers.

The method of Boschi & Ekström (2002) to derive images of the Earth's upper mantle from teleseismic observations of surface wave phase delays, in the framework of a 3-D crustal reference model, should give more reliable constraints at least on the long wavelength component of the uppermost mantle velocity structure. Here we apply it to an updated version of the data set of Ekström *et al.* (1997), and derive high resolution maps of the region underlying the Mediterranean basin, down to depths of a few hundred kilometres.

Boschi & Ekström's (2002) approach is characterized by a careful treatment of the effect of crustal heterogeneities, given as fixed parameters of the reference model. Their reference model includes the crustal structure Crust 5.1 of Mooney *et al.* (1998); we replace it with the finer Crust 2.0 (Bassin *et al.* 2000) ($2^\circ \times 2^\circ$ rather than $5^\circ \times 5^\circ$ lateral resolution).

We also modify Boschi & Ekström's (2002) parametrization, replacing their equal-area horizontal cells with two sets of equally spaced cubic splines (Wang & Dahlen 1995): a very dense one,

*Now at: ETH-Hoenggerberg/HPP 0.13, CH-8093 Zurich, Switzerland. E-mail: lapo@erdw.ethz.ch

limited to the Mediterranean, and a more sparse one to describe the rest of the globe. This choice allows us to maximize the resolution within the region of interest, with only a very limited increase in the total number of model parameters.

## 2 PARAMETRIZATION

Multiple-resolution parametrizations like ours have been designed, in recent years, by many authors attempting to integrate the results of local and global tomography (e.g. Wang *et al.* 1995; Widiyantoro & van der Hilst 1997; Bijwaard *et al.* 1998; Wang *et al.* 1998; Bijwaard 1999); for example, in Bijwaard *et al.* (1998), the extent of the cell-functions that describe the Earth's lateral velocity heterogeneity changes locally, from $6^\circ \times 6^\circ$ in areas that are not well sampled by the data, to $0.6^\circ \times 0.6^\circ$ where the data coverage is best and a high effective resolution can be achieved.

There are two main reasons to follow this approach. In the first place, the non-uniformity of the data coverage, inherent to the seismic tomographic inverse problem. Parametrizations of uniform resolution are not optimal, as they require that undersampled areas, where fine heterogeneities cannot be imaged, to be described with as many basis functions as well covered regions of equal extent; plus, if the resolution, where possible, is to be improved, the parametrization must become uniformly finer everywhere, with a large unnecessary expense of computer memory and time. A non-uniform parametrization dependent on the distribution of the data is, naturally, more efficient.

Secondly, teleseismic measurements, associated with sources located away from the region of interest, are sensitive to mantle heterogeneities outside that region. In many regional studies such heterogeneities are not free parameters of the tomographic inversion: their effect is often accounted for with some *a priori* correction, based on some 3-D global reference model; even so, inaccuracies in the global reference model are likely to map into the regional solution model, generating fictitious features. The problem is altogether avoided if the global velocity structure is also parametrized and inverted for, and the choice of a multiple density parametrization still allows us to achieve efficiently a high resolution within the region of interest.

Here we describe lateral heterogeneities in the upper mantle's transversely isotropic shear and compressional velocities in terms of a grid of 422 cubic splines (Lancaster & Salkauskas 1986; Wang & Dahlen 1995) that, globally, are approximately equally spaced, but become more densely distributed within the Mediterranean basin. Namely, 355 splines, of the 362 that result from triangulation of the globe as in Wang & Dahlen (1995), parametrize the whole solid angle; the seven splines whose centers fall within the Mediterranean basin ($-20^\circ$ to $45^\circ$E and $30^\circ$ to $50^\circ$N) are neglected and replaced by 67 splines (which are non-zero over a smaller area, and whose surface integral is accordingly smaller) defined by a three times finer triangulation (Figs 1a and b).

In the radial direction we employ the same parametrization as Boschi & Ekström (2002), consisting of nine non-equally spaced cubic splines (Fig. 1c). Smooth parametrizations like ours, as opposed to the cell basis functions used in previous, similar, studies, are more efficient in representing short wavelength structures with a relatively limited number of free parameters (Lancaster & Salkauskas 1986).

## 3 LEAST-SQUARES INVERSION

We refer to Boschi (2001) or Boschi & Ekström (2002) for a detailed formulation of the inverse problem relating transversely isotropic shear velocity anomalies in the mantle to surface wave phase delays. As in Boschi & Ekström (2002), free parameters of our inversions are relative anomalies in horizontally and vertically polarized shear wave velocities (denoted $\delta v_{SH}/v_{SH}$ and $\delta v_{SV}/v_{SV}$, respectively), and in horizontally and vertically polarized compressional velocities ($\delta v_{PH}/v_{PH}$ and $\delta v_{PV}/v_{PV}$, respectively); we assume $\delta v_{PH}/v_{PH} = \delta v_{SH}/v_{SH}$ and $\delta v_{PV}/v_{PV} = \delta v_{SV}/v_{SV}$ (Boschi & Ekström 2002), and are left with only two unknown velocity distributions, $\delta v_{SH}/v_{SH}$ and $\delta v_{SV}/v_{SV}$.

The inverse problem is based on eq. (10) of Boschi & Ekström (2002), with local JWKB (Jeffreys–Wentzel–Kramers–Brillouin, e.g. Dahlen & Tromp 1998) kernels $K'(r, \theta, \phi)$ that change depending on the local character of the (3-D) reference model. Our reference model is an improved version of the initial reference model of Boschi & Ekström (2002), in that the $5^\circ \times 5^\circ$ crustal model Crust 5.1 of Mooney *et al.* (1998) is replaced by its updated, $2^\circ \times 2^\circ$ version Crust 2.0 (Bassin *et al.* 2000), and the appropriate JWKB kernels are found for each cell of Crust 2.0. As in Boschi & Ekström (2002), the reference mantle model is 1-D, isotropic, and has no 220 km discontinuity.

Let us write the resulting inverse problem:

$$A \cdot x = d, \tag{1}$$

where the vector $x$ denotes the spline coefficients of the unknown solution model, $d$ is the phase delay data vector, and the matrix $A$ is related to sensitivity kernels and model parametrization. The number of rows of $A$ naturally coincides with the number of available phase-delay measurements (the dimension of $d$); the number of columns with the number of free parameters that describe the model (the dimension of $x$). The first $422 \times 9 = 3798$ entries of each row of $A$, and of the vector $x$ (422 being the number of horizontal basis functions, and nine the number of vertical ones), are associated with $\delta v_{SH}/v_{SH}$, the rest with $\delta v_{SV}/v_{SV}$. In both cases, the first 422 coefficients correspond to the topmost radial spline; the second 422 to the one immediately below; and so forth down to the ninth, deepest spline (Fig. 1c). Each group of 422 coefficients includes, first, the 355 coefficients of the global splines, and secondly 67 coefficients associated with the local ones. The horizontal spline index grows west to east (fast direction) and north to south. Knowing how $A$ is organized is necessary to follow our discussion of the resolution matrix, below.

In the case of a uniformly fine block parametrization, $A$ is very sparse and very large, and the most convenient way to find the least-squares solution is by means of iterative algorithms like LSQR (e.g. Boschi & Dziewonski 1999; Boschi 2001). Here, on the other hand, the upper mantle is described by a relatively limited number of overlapping cubic splines: $A$ is much smaller, but significantly denser than in Boschi & Ekström (2002). We thus find the least-squares solution $x_{LS}$ implementing directly (rather than approximating iteratively) the theoretical formula (e.g. Trefethen & Bau 1997)

$$x_{LS} = (A^T \cdot A + D)^{-1} \cdot A^T \cdot d, \tag{2}$$

where the matrix $D$, representing the cumulative effect of the regularization constraints that we impose (Boschi 2001), has the same dimensions as $A^T \cdot A$.

In order for this procedure not to be exceedingly time consuming, we do not explicitly calculate $A$; our software is designed to read the entire data set sequentially and, as each new datum is read, calculate its contribution to all entries of $A^T \cdot A$. Then, $(A^T \cdot A + D)^{-1}$ is found by a parallel implementation of Cholesky factorization, running on a multi-processor computer. The least-squares solution is thus identified much faster than it would have been in a single-processor LSQR iterative approximation (Boschi 2003).

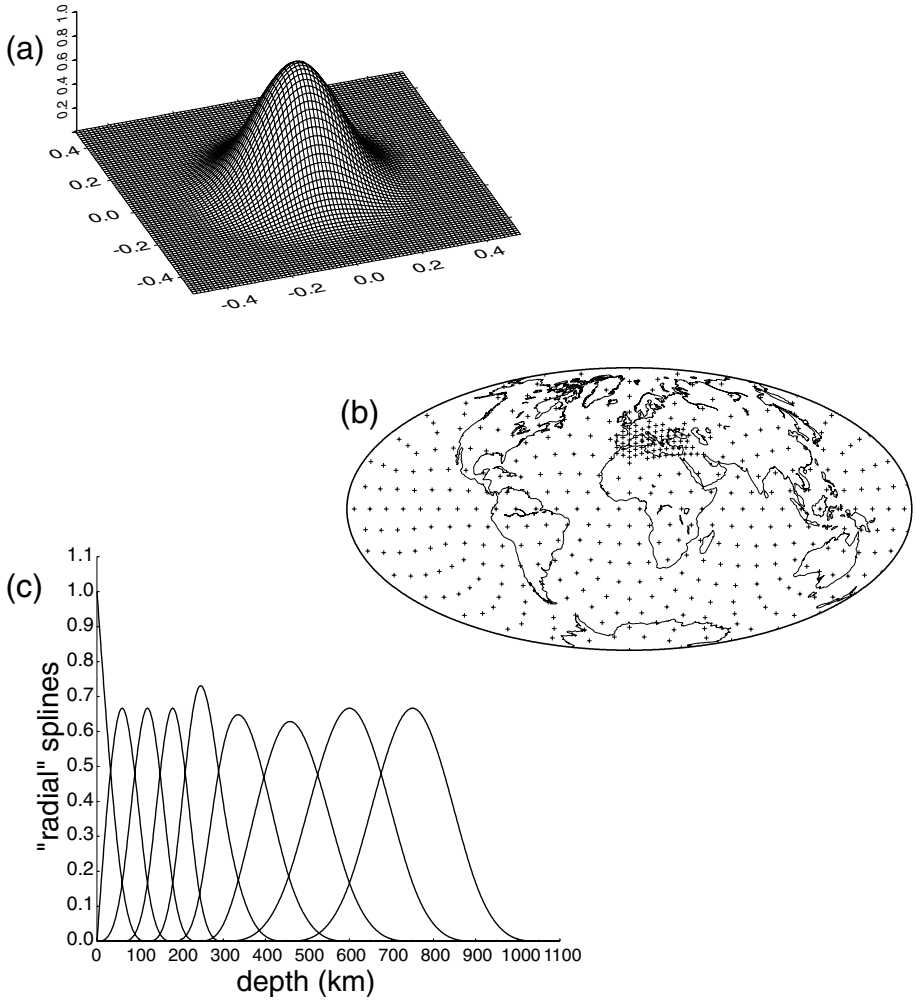


**Figure 1.** (a) The cubic spline horizontal basis function. (b) Centers of the cubic splines that describe lateral variations of $v_{SH}$ and $v_{SV}$ in our parametrization. (c) Radial cubic splines that describe radial variations of $v_{SH}$ and $v_{SV}$.

## 4 RESOLUTION

In most seismic tomography studies, the resolution, or spatial extent of the smallest seismic velocity anomaly that can possibly be imaged, is typically evaluated through synthetic tests: given the data coverage (geographic distribution of sources and stations for which measurements are available), ray-theoretical traveltimes in a given velocity model (e.g. a checkerboard function) are calculated for each ray path; a synthetic data set is thus assembled, and inverted with the same algorithm used to invert real seismic data. The similarity of the solution model to the one from which synthetic data were computed is a measure of the completeness of the data set: in the ideal case of perfect coverage, the input and output model should coincide (e.g. Boschi & Dziewonski 1999).

In this procedure, the same theoretical formulation (JWKB ray theory) is generally used both to solve the forward problem and to formulate the inverse problem. Limits in resolution that arise from the approximations involved in the theory are therefore ignored.

Here, as we attempt to constrain fine seismic structure from relatively long period measurements, the use of JWKB ray theory might be more limiting than non-uniformities in the data coverage. We shall give careful consideration to both issues.

### 4.1 Theoretical limits

JWKB ray theory strictly holds in the limit of infinite frequency. Close to this limit, the shape of a ray path and the traveltime of a seismic phase propagating along that ray path, only depend on the value of seismic velocities on the ray path itself.

Seismic waves at finite frequencies, on the other hand, are affected by velocity structure away from the JWKB ray path. This effect has been investigated (through scattering, or Born, theory) for example by Marquering *et al.* (1999), Dahlen *et al.* (2000), Hung *et al.* (2000), Spetzler *et al.* (2001, 2002), and Zhou *et al.* (2003).

When we use JWKB ray theory to formulate a seismic inverse problem associated with data of relatively low frequency, we are implicitly limiting the spatial resolution of the solution; in practice, velocity anomalies distributed on a banana–doughnut-shaped sensitivity kernel (i.e. the Fréchet derivative) surrounding the ray path are fictitiously mapped onto the ray path itself. The authors mentioned above find banana–doughnut sensitivity kernels from a comparison of wavefields derived with JWKB ray theory, and scattering theory in the Born or Rytov approximations. If we accept their treatment, we can estimate the resolution achieved by the JWKB ray theory formulation, based upon the size of the

banana–doughnuts (or of the Fresnel zone): the larger the doughnuts (or the Fresnel zone), the lower the resolution.

Spetzler *et al.* (2001) state, for example, that the lateral size of the smallest anomaly resolvable by 40 s Love waves in the JWKB approximation, be of *ca* 1300 km. This value roughly corresponds to the maximum diameter of the banana–doughnut associated with a teleseismic (epicentral distance of 30°) Love wave at a similar frequency, as derived by Marquering *et al.* (1999, fig. 7).

We suggest that this estimate of resolution may be somewhat too conservative. The area over which Fréchet kernels are non-zero tends to zero near source and receiver; hence, the resolution of a surface wave data set might be very high in a region densely covered with sources and stations. In general, the results presented below favour a more optimistic view.

[Naturally, theoretical limits to resolution could be surpassed by dropping JWKB theory and accounting for finite frequency effects, by scattering theory (e.g. Spetzler *et al.* 2002), normal mode theory (e.g. Woodhouse & Girnius 1982; Clévédé & Lognonné 1996; Tanimoto 2003), or numerical calculations (e.g. Komatitsch & Tromp 1999; Tape 2003), but this goes beyond the purposes of the present work.]

## 4.2 Resolution matrix

That the above mentioned synthetic, or checkerboard tests are only of limited usefulness has been noted, for example, by Lévêque *et al.* (1993). Here, we quantify resolution in a more rigorous fashion. After finding explicitly the generalized inverse matrix $(A^T \cdot A + D)^{-1}$, we can readily determine the resolution matrix (section 4.5.1 in Menke 1989; Boschi 2003):

$$R = (A^T \cdot A + D)^{-1} \cdot A^T \cdot A. \tag{3}$$

In the ideal case of perfect resolution, $R$ should equal the identity matrix $I$; differences between $R$ and $I$ tell us about fictitious effects involved in the least-squares inversion.

Calculating $R$ is, in a sense, equivalent to performing a resolution test (the output model vector can be found by simply dot-multiplying $R$ by the input model vector); however, the direct analysis of $R$ can lead to more general conclusions, as it does not involve biases that are necessarily introduced by the choice of the input model.

We find the resolution matrix $R$ associated with the entire phase velocity data set of Boschi & Ekström (2002), except for the major arc observations, therefore, in this study we choose to ignore it (see next section). The regularization matrix $D$ is, naturally, that applied to the least-squares inversion that lead to our preferred solution, as discussed in the next section.

### 4.2.1 *Trade-offs between $\delta v_{SH}/v_{SH}$ and $\delta v_{SV}/v_{SV}$*

The resolution matrix $R$ is too large to be plotted entirely, and with full resolution, in one single figure. For each $18 \times 18$ block of $R$, we sum all entries and divide by 18: ideally, the resulting values should equal one along the diagonal and zero elsewhere. We show this filtered version of $R$ in Fig. 2.

From the above description of $A$, we know that the upper left $3798 \times 3798$ diagonal block of $R$ describes how the data can resolve

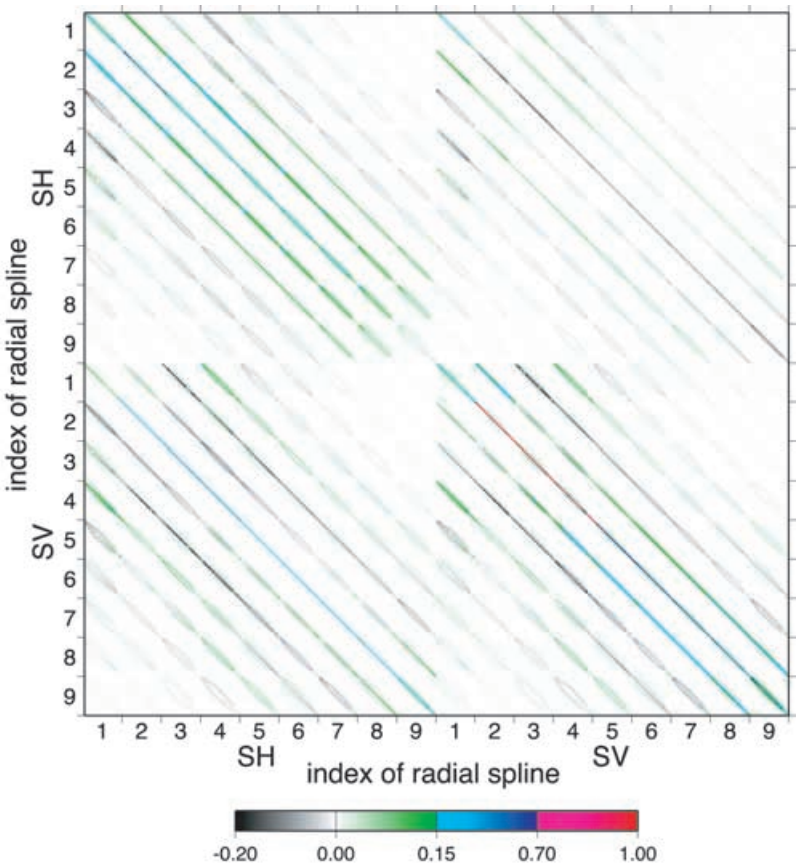


**Figure 2.** Model resolution matrix $R$ from phase velocity data. In order to plot the entire matrix in a single page we had to smooth it: each pixel of this image represents $18 \times 18$ pixels of $R$. With *SH* and *SV* we denote the matrix elements associated with horizontally and vertically polarized shear velocity, respectively.

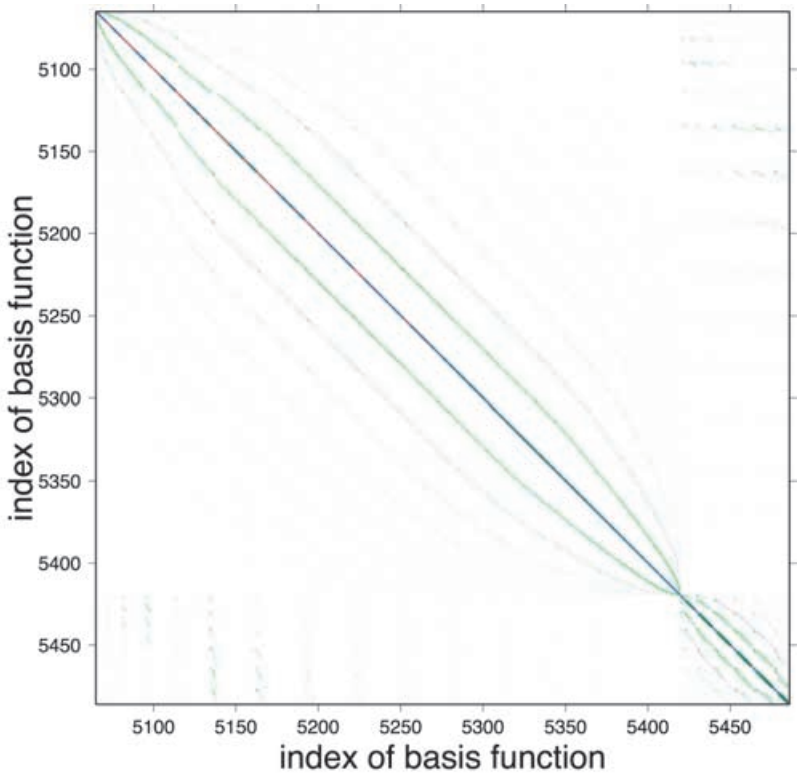


**Figure 3.** Twelfth 422 × 422 diagonal block of $R$ (not smoothed), showing how well we can resolve coefficients of $\delta v_{SV}$ associated with the third shallowest radial spline.

$\delta v_{SH}/v_{SH}$, while its lower right diagonal 3798 × 3798 diagonal block corresponds to $\delta v_{SV}/v_{SV}$. All non-zero entries in the other two blocks (upper right and lower left) identify fictitious trade-offs in the solution between $\delta v_{SH}/v_{SH}$ and $\delta v_{SV}/v_{SV}$.

Because Love waves are almost only sensitive to heterogeneities in $v_{SH}$, and Rayleigh waves are much more sensitive to $\delta v_{SV}/v_{SV}$ than to $\delta v_{SH}/v_{SH}$ (e.g. Boschi & Ekström 2002), under normal conditions the $v_{SH}$ and $v_{SV}$ components of the solution are strongly decoupled, and, accordingly, all entries in the two 3798 × 3798 off-diagonal blocks of $R$ are approximately zero. Here, however, we have chosen to put a strong damping on the anisotropy of the solution (see Section 5.1 below), and an artificial coupling between $\delta v_{SH}/v_{SH}$ and $\delta v_{SV}/v_{SV}$ results, evidenced by the presence of non-zero diagonal bands in the off-diagonal blocks.

#### *4.2.2 Vertical trade-offs*

Within the two 3798 × 3798 diagonal blocks of $R$, non-zero diagonal bands separated by 421 entries that are approximately zero indicate a trade-off between model coefficients associated to neighboring radial splines: JWKB sensitivity kernels are usually non-zero over large depth ranges within the upper mantle, making it relatively hard to resolve the radial dependence of velocity heterogeneities.

Fig. 2 also evidences a certain decay of resolution with increasing depth of the radial spline basis functions. We shall later show tomographic images extending to depths of *ca* 800 km, but only fully trust them down to *ca* 400 km.

The loss of resolution with increasing depth is particularly fast in the case of $v_{SH}$ anomalies (upper left 3798 × 3798 diagonal block): Love wave sensitivity functions (most important to constrain $\delta v_{SH}/v_{SH}$) are non-zero within a more limited, and shallower, depth range than Rayleigh wave ones.

#### *4.2.3 Lateral trade-offs*

Horizontal trade-offs are more limited than radial ones, owing to the relatively uniform geographic distribution of observations in our data set. To have a closer look, we plot in Fig. 3 the twelfth 422 × 422 diagonal block of $R$, associated with the third shallowest radial spline in the parametrization of $\delta v_{SV}/v_{SV}$. Each pixel now represents one entry of $R$. This portion of $R$, corresponding to a well resolved (though not the best resolved) depth range in the upper mantle, is strongly diagonal, with diagonal entries very close to one. Non-zero off-diagonal entries are few and small, proving that horizontal trade-offs are almost negligible. In Fig. 3 they are organized in elliptical patterns, because of the distribution and indexing of horizontal basis functions; a separate set of non-zero off-diagonal ellipses is associated with the last 67 diagonal entries, corresponding to the denser subset of cubic splines that describe the Mediterranean region; the latter portion of $R$ has the same properties as the rest of the matrix, and we infer that our choice of a finer parametrization for the Mediterranean is legitimate.

The properties of Fig. 3 are shared by all other analogous 422 × 422 blocks of $R$, corresponding to either $v_{SH}$ or $v_{SV}$ and to all radial splines. In all cases non-zero matrix elements are strongly concentrated on the diagonal. Particularly for the $v_{SH}$ part of the matrix, the size of diagonal entries decreases with increasing depth of the radial spline, as relatively few data are sensitive to $v_{SH}$ anomalies in the transition zone and upper mantle.

Except for those associated with the deepest radial splines, non-diagonal entries in Figs 2 and 3 are all substantially smaller than the

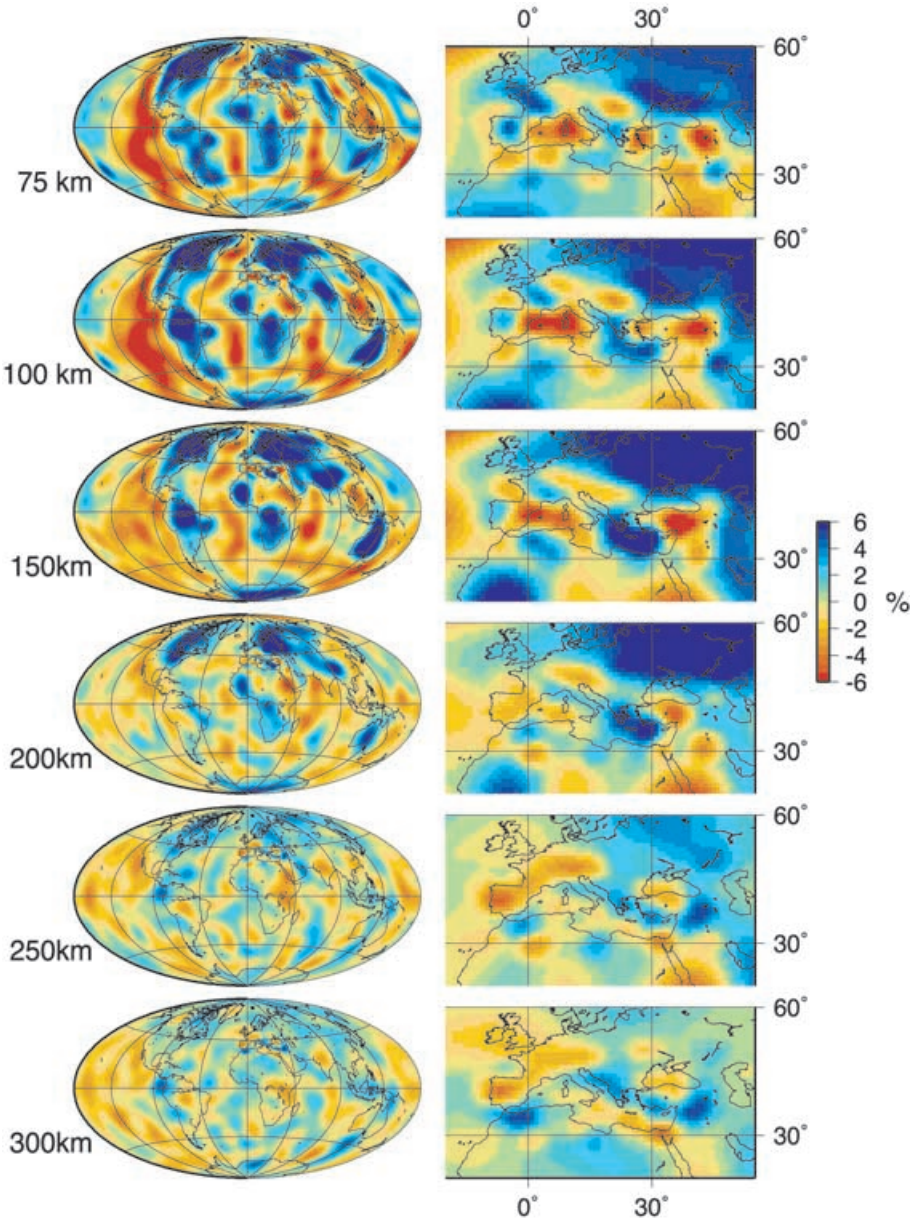


**Figure 4.** Global (left) and regional (right) maps of $\delta v_S/v_S$, from the Voigt average $2/3\delta v_{SV}/v_{SV} + 1/3\delta v_{SH}/v_{SH}$, at the six indicated depths in the upper mantle.

corresponding diagonal ones, proving that the radial data coverage is adequate to the chosen parametrization.

## 5 SHEAR VELOCITY IN THE UPPER MANTLE

Our preferred maps of $\delta v_{SV}/v_{SV}$ and $\delta v_{SH}/v_{SH}$, whose Voigt average (e.g. Ekström & Dziewonski 1998) we show in Fig. 4, were obtained from the simultaneous inversion of the entire data set of Boschi & Ekström (2002), with the exception of the small number of measurements associated with surface waves travelling along major arcs, which we have decided to ignore: the corresponding ray paths being very long, the sensitivity of these data to lateral heterogeneities is non-zero over a wide area (e.g. fig. 1 in Spetzler *et al.* 2001; Zhou *et al.* 2004) and this limits their resolution of lateral structure.

### 5.1 Regularization

Preliminary undamped or weakly damped inversions of the full data set failed, because $A^T \cdot A$ is ill-conditioned, or resulted in solution models with a short-wavelength component too strong for the expected resolution. We have therefore looked for the optimal damping scheme, with a number of inversions where we have minimized the norm of the solution, and the difference between $\delta v_{SV}/v_{SV}$ and $\delta v_{SH}/v_{SH}$. We have decided to discard roughness minimization as a regularization criterion, because of its tendency to penalize small scale features, within the high resolution region, that appear to be meaningful. We have weighted the rows of the norm damping matrix based upon the volume of the horizontal and vertical splines (smaller, and denser, splines are damped less), but found this endeavour to affect the solution only slightly, at least at the level of damping that we have chosen.

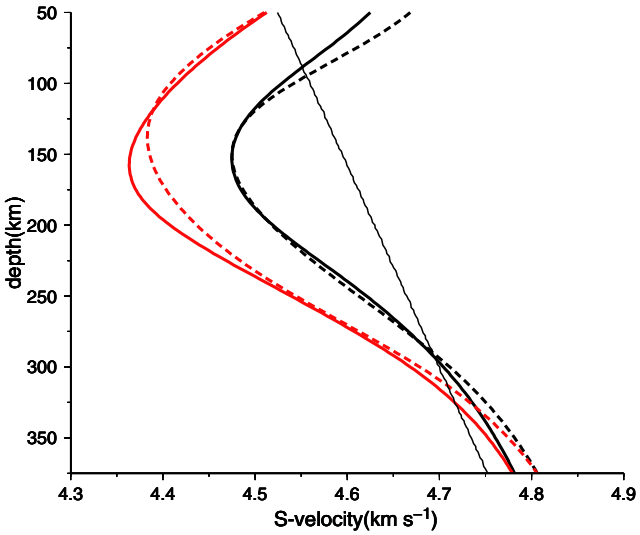


**Figure 5.** Mean values of $v_{SV}$ (red curves) and $v_{SH}$ (thick black) as a function of depth, from the model of Figs 4 and 5. The solid curves are found averaging the values of $v_{SV}$ and $v_{SH}$, at all depths, throughout the globe. The dashed curves are found if the average is restricted to the Mediterranean basin.

Because of the decoupling between the $v_{SV}$ and $v_{SH}$ components of the solution, mentioned in Section 4.2 above, inversions with no minimization of $\delta v_{SV}/v_{SV} - \delta v_{SH}/v_{SH}$ tend to produce strongly anisotropic images, but the accuracy of the mapped anisotropy is dubious; with the regularization scheme chosen here we are more likely to image lateral anomalies in radial anisotropy that are physically significant.

### 5.2 Discussion

Before plotting the Voigt average of $\delta v_{SV}/v_{SV}$ and $\delta v_{SH}/v_{SH}$ in Fig. 4, we subtract their average value at all depths; the 1-D deviation of the solution from the starting model can be seen in Fig. 5, where we show the mean values of $v_{SV}$ and $v_{SH}$, resulting from our inversion, as a function of depth. As was to be expected, the behaviour of the globally averaged (black curves) $v_{SV}$ and $v_{SH}$ as functions of depth is analogous to that observed by (Boschi & Ekström 2002), with a region of minimum velocity (and maximum anisotropy) at *ca* 150 km; the average values of $v_{SV}$ and $v_{SH}$ calculated for the Mediterranean only are similar to the global ones, probably reflecting the fact that this region (as we have defined it here) includes an almost equal share of continental, cratonic and oceanic areas.

The global pattern of shear velocity anomalies in Fig. 4 (left panels) is similar to those of Boschi (2001, chapter 6) and Boschi & Ekström (2002), dominated by the signature of deep continental roots and mid-oceanic ridges. Within the Mediterranean basin (right panels), lateral $v_S$ structure in the top *ca* 150 km of the upper mantle is characterized by several prominent features that can be explained on the basis of the region's tectonic history (e.g. de Jonge *et al.* 1994, figs 14 and 15):

(i) The fast roots of the Iberian peninsula.

(ii) A well defined fast anomaly, most likely associated with subduction, underlying (at all depths considered here) the Adriatic sea and Aegean arc.

(iii) A large-scale low-velocity anomaly extending throughout the western Mediterranean, corresponding to the known tectonic extension of the area.

(iv) A shallow, slow anomaly of the same origin under the Aegean sea.

(v) A strong slow anomaly extending from the Moho to *ca* 200 km depth under the Turkish–Iranian continental plateau, already mapped by a number of authors (e.g. Villaseñor *et al.* 2001, fig. 9) and associated by Villaseñor *et al.* (2001) to the collision between the Arabian and Eurasian plates.

At 250–300 km depth, the $v_S$ map is dominated by a fast anomaly of linear shape running under Anatolia, the Balkans, Italy and northwestern Africa. de Jonge *et al.* (1994) have shown that, in this depth range, a similar velocity structure is to be expected based upon a tectonic reconstruction of the temperature field. The consistency between our maps and their result (Fig. 6), also substantiated by tomographic images derived from body wave measurements (e.g. Bijwaard 1999), suggests that our data set might achieve a resolution of lateral structure better than expected from the considerations of Spetzler *et al.* (2001) (see above).

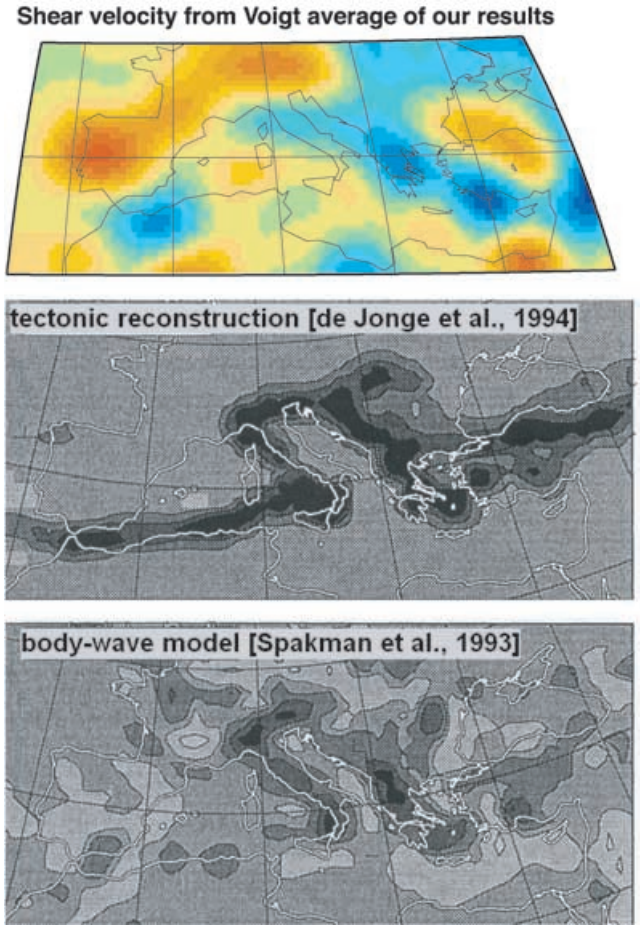


**Figure 6.** A comparison, at 245 km depth, between our results (top panel, same color scale as Fig. 4), de Jonge *et al.* (1994) computed *P*-wave velocity structure, based upon Dercourt *et al.* (1986) tectonic reconstruction (middle panel), and Spakman *et al.* (1993) tomographic image, derived from *P*-wave traveltime observations (bottom panel). The middle and bottom panels are taken from de Jonge *et al.* (1994): their gray-scale ranges from −2.5 per cent (light gray) to 2.5 per cent (black).

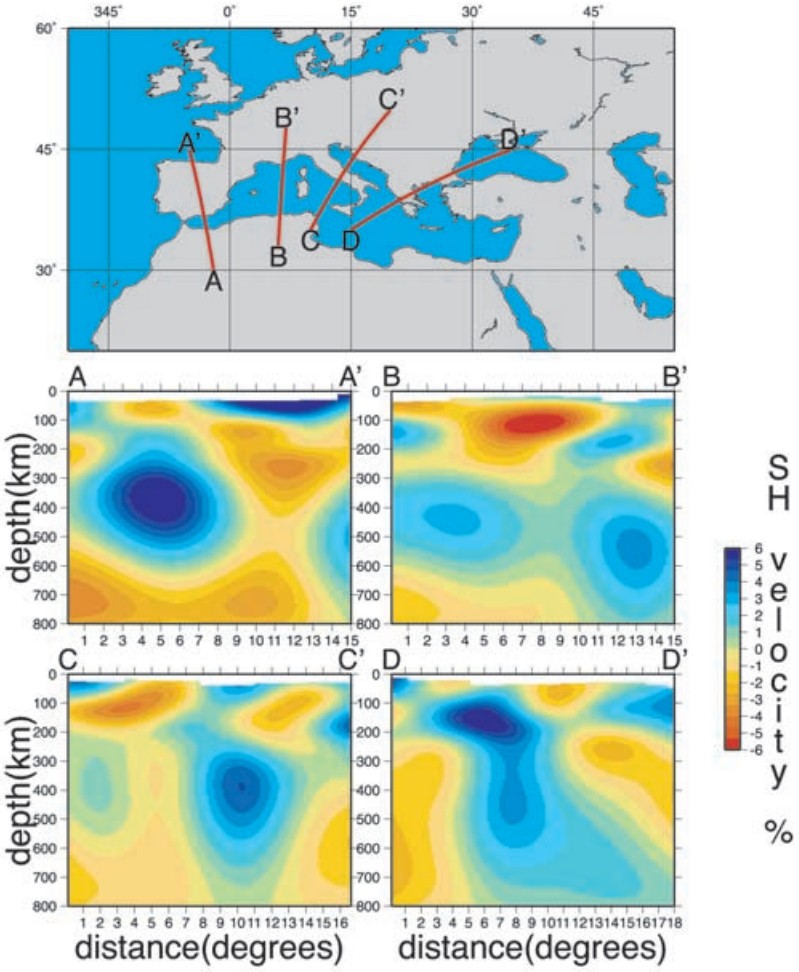


**Figure 7.** Vertical sections through the Voigt average $\delta v_S/v_S$ of our model, cut along the red lines shown on the map. Capital letters (A and A′, B and B′ and so forth) denote the sections' endpoints. The white layer at the top of each section represents the crust; note the strong lateral variations in the depth of the Moho (from Crust 2.0).

Fig. 6 also shows that some features that were not predicted by the simplified model of de Jonge *et al.* (1994) are, nevertheless, shared by our map and that of Spakman *et al.* (1993) (bottom panel of Fig. 6): in particular, the low velocity anomalies under Iberia, central Europe, the Black sea and southeastern Mediterranean.

Vertical sections (Fig. 7) of the Mediterranean upper mantle and transition zone are also dominated by fast anomalies associated with the subduction of Africa under Eurasia. Subducting slabs are imaged under the Iberian peninsula (section AA′), the western Mediterranean (BB′) and the Aegean arc (DD′). Fast anomalies which were possibly originated by past subduction are present under the Alps (BB′) and the Adriatic sea (CC′). The vertical gradient of $\delta v_S/v_S$ appears from Fig. 7 to be maximum at depths of *ca* 100 and *ca* 300 km, where there appears to be a change in the shape of subducting slabs. We were not able to distinguish a clear image of the Calabrian arc subduction, whose lateral extent might be too small for our resolving power.

At depths larger than *ca* 400 km, the scale length of our images rapidly increases: seismic velocity in the lower portion of the upper mantle is only constrained by longer period observations (e.g. Boschi & Ekström 2002) that are less numerous, and strongly are affected by the theoretical limitations described in Section 4.1 (the size of the Fresnel zone grows with the period). In this depth range, our images should then be viewed as a low-pass filtered version of true Earth structure.

In Fig. 8 we compare our western Mediterranean cross-section with two analogous (*P*-wave velocity) sections taken, again, from de Jonge *et al.* (1994). The long-wavelength component of all images is in agreement, showing low velocities in the shallow mantle underlying the sea bottom, and fast anomalies associated with past and current subduction, under the Alps and northern Africa. The anomaly under the Alps appears to be divided into three sections, with large vertical gradients at *ca* 150 and *ca* 300 km depth, both in our surface wave based image and in the body wave one of Spakman *et al.* (1993) (Fig. 8 middle panel, labelled EUR89B). In the reconstruction of de Jonge *et al.* (1994) (Fig. 8 bottom panel, labelled DRW), the same feature has, instead, a continuous character. The consistency between two tomographic models derived from profoundly different observations suggests that, for what concerns this particular region, de Jonge *et al.* (1994) approach might be oversimplified.

The very top of the upper mantle under the western Mediterranean is characterized, in the Spakman *et al.* (1993) map, by a strong fast anomaly, absent from both our image and de Jonge *et al.* (1994) reconstruction. While Spakman *et al.* (1993) have formulated their inverse problem assuming a crustal layer of uniform properties, the

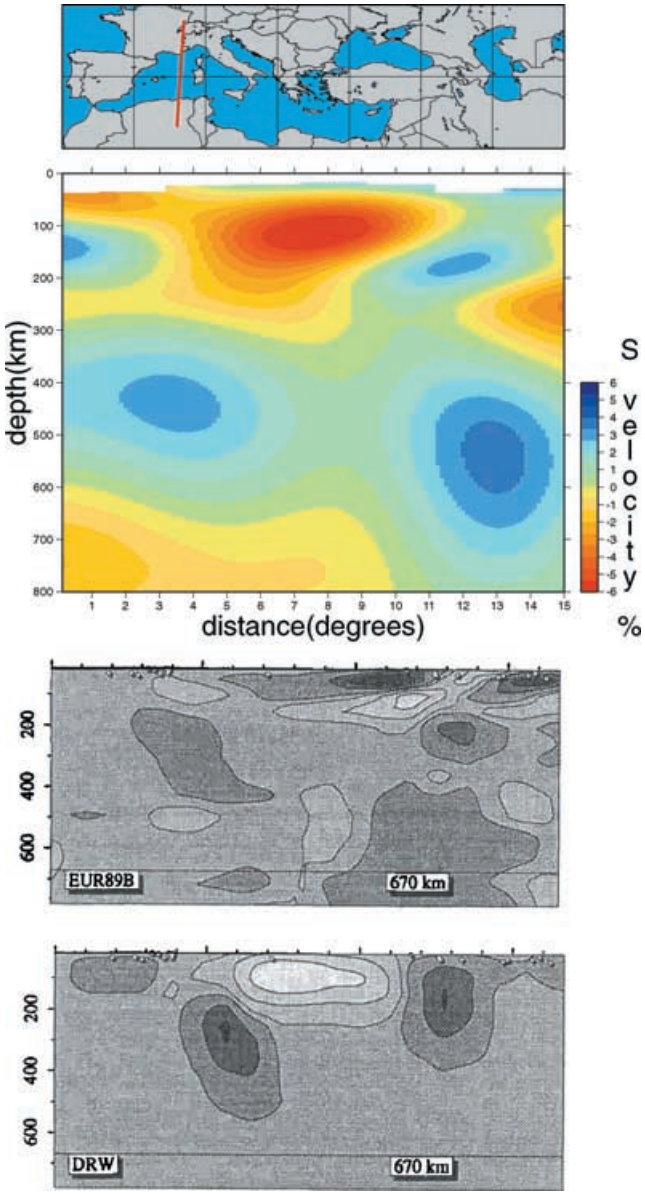


**Figure 8.** Vertical section BB′ (left = south, right = north) of western Mediterranean seismic velocity structure, from three different models: *S*-wave velocity variations from the Voigt average of our results (top panel); Spakman *et al.* (1993) *P*-wave velocity model (middle panel); de Jonge *et al.* (1994) computed *P*-wave velocity structure, based upon Dewey *et al.*'s (1989) tectonic reconstruction (bottom panel).

crust under the Mediterranean sea is known to be thinner than average (Figs 7 and 8); the delay of *P*-wave traveltimes introduced by the crust is then overestimated, and a region of fictitiously high velocity is likely to be mapped into the mantle as a result. Alternatively, the unexpected fast anomaly could be simply explained by the absence of seismic sources and stations in the area, and the subsequent lack of shallow-travelling body wave rays, and resolution. Surface wave observations are more effective than body wave ones in constraining the shallowest upper mantle structure, particularly if lateral heterogeneities in crustal structure are accurately accounted for.

Fig. 9 shows how well the starting model and the solution discussed above reduce the variance of Rayleigh and Love wave data with respect to PREM (Preliminary Reference Earth Model, Dziewonski & Anderson 1981). The starting model, which does not account for radial anisotropy of the upper mantle, does not achieve a positive fit of Rayleigh wave and longer period Love wave data. The solution model reduces the variance of both Love and Rayleigh wave data as well as solutions derived with no minimization of radial anisotropy: this justifies our choice of regularizing the inverse problem by coupling $\delta v_{SV}/v_{SV}$ and $\delta v_{SH}/v_{SH}$. As to be expected, since the total number of free parameters is much smaller, the data fit is not better than that of Boschi & Ekström (2002).

As in Boschi & Ekström (2002), we have iterated our procedure, using the 3-D model discussed here as the starting point for a new inversion; in this process, we have accordingly corrected all the local JWKB sensitivity kernels. The solution remains stable: perturbations are small and of limited spatial extent, and only involve areas of relatively poor resolution (depths of 200 km or more).

## 6 RADIAL ANISOTROPY

We now compute the difference between our maps of $\delta v_{SV}/v_{SV}$ and $\delta v_{SH}/v_{SH}$, and show it in Fig. 10 after having subtracted its average value at each depth. As noted above, in the least-squares inversion that lead to this solution we had minimized the difference between $v_{SV}$ and $v_{SH}$; nevertheless, our global maps confirm once again the presence of a strong anomaly in radial anisotropy under the central Pacific, with the same character as found by Ekström & Dziewonski (1998).

Within the Mediterranean basin and surrounding regions, lateral variations in radial anisotropy are not as strong, and do not have such a significant long spatial wavelength component. A relatively prominent anomaly in radial anisotropy, with $\delta v_{SV}/v_{SV} < \delta v_{SH}/v_{SH}$, interests the uppermost mantle (75–100 km depth) underneath Saharan Africa: it is mirrored, within the same depth range, by an anomaly of the same sign under the Pyrenees, northwestern France and the Balkans, which seems to continue through the Aegean sea and Anatolia. Similar anomalies exist under the Horn of Africa (maximum at *ca* 100 km depth) and Iran (*ca* 150 km). Anisotropic anomalies of the opposite sign are present under the eastern Mediterranean and Black sea, extending to depths of *ca* 200 km.

Our resolution of radial anisotropy is limited by the difference in quality and coverage of Love vs. Rayleigh wave observations, the first being most sensitive to $v_{SH}$, the second to $v_{SV}$. This is particularly true at depths larger than, say, *ca* 150 km, almost exclusively sampled by Rayleigh waves. In addition, significant discrepancies exist between various estimates of the thickness of the sediment layer in the shallow crust (Tkalčić & Laske 2002), and fictitious vertical trade-offs are not unlikely (Boschi & Ekström 2002). Anisotropic anomalies like those of Fig. 10 are particularly hard to resolve, and must be seen with the understanding that further, seismological and geodynamic research is needed to assess their quality.

## 7 CONCLUSIONS

We have found that reliable long-wavelength regional images of the upper mantle can be derived from a large set of teleseismic measurements of surface wave phase velocity. The inherently long-wavelength character of the data, and the choice of a multiple-resolution parametrization, allow us to minimize the number of free parameters that describe the solution: it is then feasible to find directly the model resolution matrix $R$ to evaluate the adequacy of data coverage (Boschi 2003). Fictitious trade-offs in the solution

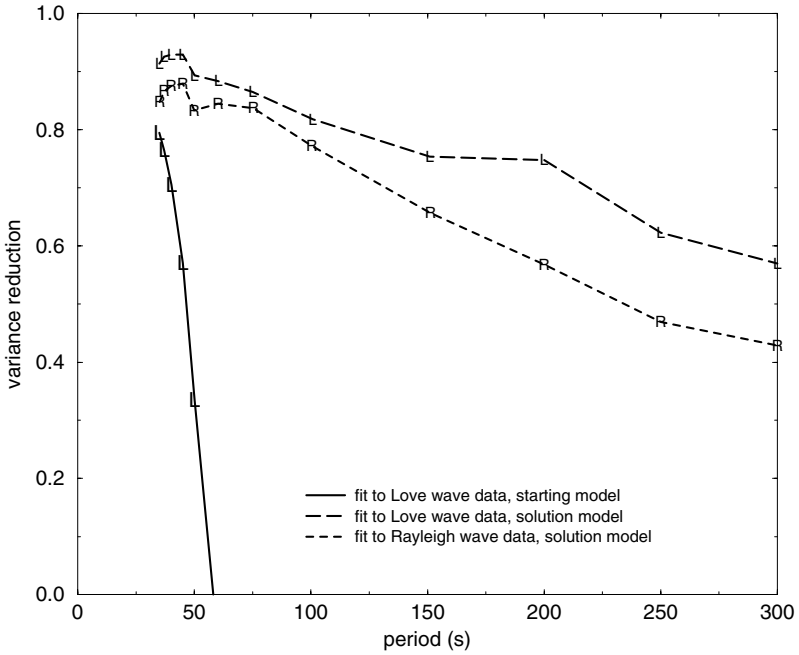


**Figure 9.** Variance reduction of Rayleigh and Love wave phase velocity data achieved by our 3-D model and by the starting model with respect to PREM. Measurements are subdivided according to the surface wave periods, and variance reduction is computed separately for each period. The starting model, that does not account for upper mantle anisotropy, does a worse job than PREM explaining Rayleigh wave phase velocity data (systematically negative variance reduction). Because its crustal structure (Crust 2.0) is well constrained, it reduces the variance of shorter-period Love wave phase velocity data.

are small and, owing to the smooth, long-wavelength character of JWKB radial sensitivity functions, they are limited to the radial direction.

We have verified that our images of the upper mantle reproduce well the pattern of fast and slow anomalies expected from tectonic reconstructions. This is true even at fairly short spatial wavelengths (compare, for example, Fig. 4 here with fig. 16 of de Jonge *et al.* 1994), suggesting that, at least in a region densely covered by seismic sources and stations, the lateral resolution achieved by surface wave data might be somewhat better than that suggested by theoretical studies (Marquering *et al.* 1999; Spetzler *et al.* 2001).

Our method differs from those employed in other regional surface wave tomographic studies (e.g. Snieder 1988; Villaseñor *et al.* 2001; Paysanos & Walter 2002) in that it accounts for the non-linear effect of seismic velocity heterogeneities on surface wave JWKB sensitivity kernels (Boschi & Ekström 2002). We find that crustal, rather than mantle, heterogeneities affect the kernels most: after a first inversion (from a starting model that includes a 1-D mantle and a laterally varying crust), we updated the sensitivity kernels, accounting for lateral heterogeneities in the mantle, and found them to differ only slightly from those derived in the starting model. Accordingly, and in agreement with that noted by Boschi & Ekström (2002), the subsequent iteration of our inversion algorithm has not resulted in strong further corrections to the previous solution.

Once the multiple (and non-linear) effects of crustal heterogeneity are thus accounted for, intermediate-period surface wave data are the most efficient means to image the global lateral structure of the upper mantle, at spatial wavelengths of a few hundred kilometres and more. In fact, teleseismic body wave traveltimes are not sensitive to the Earth's structure in this depth range, except for the small regions immediately underlying seismic sources and receivers, and regional body wave observations are difficult to make and more sensitive to non-linearities that are systematically neglected (ray bending).

Images like ours are then a natural starting point for higher resolution tomographic inversions of body wave data, optimizing model quality at all spatial wavelengths.

## ACKNOWLEDGMENTS

Thanks to T. Becker, W. Debski, A. Dziewonski, P. Gasparini, D. Giardini, Y. Gu, S. Judenherc, L. Marques, G. Nolet, C. Piromallo, J. Trampert, A. Zollo and an anonymous reviewer. The *PhD thesis* of L. Boschi (Boschi 2001) is available on-line: http://www.seismology.harvard.edu/∼boschi, or http://people.na.infn.it/∼boschi. Details on the crustal model Crust 2.0 are given on the Reference Earth Model (REM) web-page: http://mahi.ucsd.edu/Gabi/rem.html. Most figures were prepared with GMT (Wessel & Smith 1991).

## REFERENCES

Bassin, C., Laske, G. & Masters, G., 2000. The current limits of resolution for surface wave tomography in North America, *EOS, Trans. Am. geophys. Un.,* **81**, F897.

Bijwaard, H., 1999. Seismic travel-time tomography for detailed global mantle structure, thesis, Utrecht University, Netherlands.

Bijwaard, H., Spakman, W. & Engdahl, E.R., 1998. Closing the gap between regional and global travel-time tomography, *J. geophys. Res.,* **103**, 30 055–30 078.

Boschi, L., 2001. Applications of linear inverse theory in modern global seismology, PHD thesis, Harvard University, Cambridge, MA.

Boschi, L., 2003. Measures of resolution in global body wave tomography, *Geophys. Res. Lett.,* **30**, 1978, doi:10.1029/2003GL018222.

Boschi, L. & Dziewonski, A.M., 1999. 'High' and 'low' resolution images of the Earth's mantle: Implications of different approaches to tomographic modeling, *J. geophys. Res.,* **104**, 25 567–25 594.

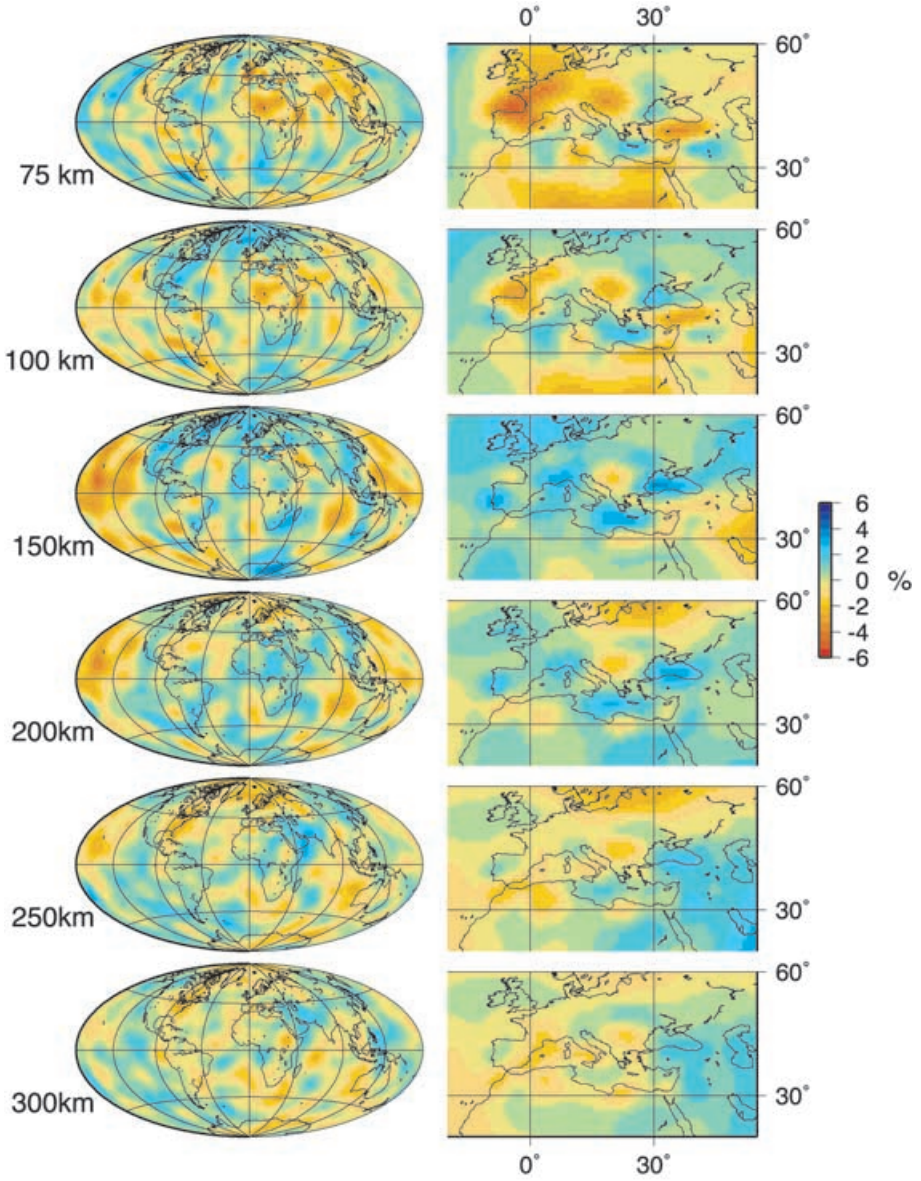


**Figure 10.** Global (left) and regional (right) maps of radial anisotropy $\delta v_{SV}/v_{SV} - \delta v_{SH}/v_{SH}$ in our model.


Boschi, L. & Ekström, G., 2002. New images of the Earth's upper mantle from measurements of surface-wave phase velocity anomalies, *J. geophys. Res.,* **107**, doi:10.129/2000JB000059.

Clévédé, E. & Lognonné, P., 1996. Fréchét derivatives of coupled seismograms with respect to an anelastic rotating earth, *Geophys. J. Int.,* **124**, 456–482.

Dahlen, F.A., Hung, S.-H. & Nolet, G., 2000. Fréchet kernels for finite-frequency traveltimes—I. Theory, *Geophys. J. Int.,* **141**, 157–174.

Dahlen, F.A. & Tromp, J., 1998. Theoretical Global Seismology, Princeton University Press, Princeton, NJ.

de Jonge, M.R., Wortel, M.J.R. & Spakman, W., 1994. Regional scale tectonic evolution and the seismic velocity structure of the lithosphere and upper mantle: The Mediterranean region, *J. geophys. Res.,* **99**, 12 091–12 108.

Dercourt, J. et al, 1986. Geological evolution of the Tethys from the Atlantic to the Pamirs since the Lias, *Tectonophysics,* **123**, 241–315.

Dewey, J.F., Helman, M.L., Turco, E., Hutton, D.H.W. & Knott, S.D., 1989. Kinematics of the western Mediterranean, in, *Alpine Tectonics,* **45**, pp. 265–283, eds Coward, M.P., Dietrich, D. & Park, R.G., *Spec. Pub., Geol. Soc. Lond*.

Dziewonski, A.M. & Anderson, D.L., 1981. Preliminary reference Earth model, *Phys. Earth planet. Int.,* **25**, 297–356.

Ekström, G. & Dziewonski, A.M., 1998. The unique anisotropy of the Pacific upper mantle, *Nature,* **394**, 168–172.

Ekström, G., Tromp, J. & Larson, E.W.F., 1997. Measurements and global models of surface wave propagation, *J. geophys. Res.,* **102**, 8137–8157.

Faccenna, C., Becker, T.W., Lucente, F.P., Jolivet, L. & Rossetti, F., 2001. History of subduction and back-arc extension in the Central Mediterranean, *Geophys. J. Int.,* **145**, 1–21.

Hung, S.-H., Dahlen, F.A. & Nolet, G., 2000. Fréchet kernels for finite-frequency traveltimes—II. Examples, *Geophys. J. Int.,* **141**, 175–203.

Komatitsch, D. & Tromp, J., 1999. Introduction to the spectral-element method for 3-D seismic wave propagation, *Geophys. J. Int.,* **139**, 806–822.

Lancaster, P. & Salkauskas, K., 1986. *Curve and surface fitting—An introduction,* Academic Press, San Diego.

Lévêque, J.J., Rivera, L. & Wittlinger, G., 1993. On the use of the checkerboard test to assess the resolution of tomographic inversions, *Geophys. J. Int.,* **115**, 313–318.

Marquering, H., Dahlen, F.A. & Nolet, G., 1999. Three-dimensional sensitivity kernels for finite-frequency travel times: the banana-doughnut paradox, *Geophys. J. Int.,* **137**, 805–815.

Menke, W., 1989. *Geophysical Data Analysis: Discrete Inverse Theory,* rev. edn, Academic Press, San Diego, CA.

Mooney, W.D., Laske, G. & Masters, G., 1998. CRUST-5.1: A global crustal model at 5° × 5 deg, *J. geophys. Res.,* **103**, 727–747.

Paysanos, M.E. & Walter, W.R., 2002. Crust and upper mantle structure of North Africa, Europe, and the Middle East from inversion of surface waves, *Geophys. J. Int.,* **149**, 463–481.

Piromallo, C. & Morelli, A., 1997. Imaging the Mediterranean upper mantle by P-wave travel time tomography, *Ann. Geofis.,* **40**, 963–979.

Piromallo, C. & Morelli, A., 2003. P-wave tomography of the mantle under the Alpine-Mediterranean area, *J. geophys. Res.,* **108**, doi:10.1029/2002JB001757.

Shearer, P.M., 1999. *Introduction to Seismology,* Cambridge University Press, Cambridge, UK.

Snieder, R., 1988. Large scale waveform inversions of surface waves for lateral heterogeneity–II: Application to surface waves in Europe and the Mediterranean, *J. geophys. Res.,* **93**, 12 067–12 080.

Spakman, W., van der Lee, S. & van der Hilst, R.D., 1993. Travel-time tomography of the European-Mediterranean mantle down to 1400 km, *Phys. Earth planet. Int.,* **79**, 3–74.

Spetzler, J., Trampert, J. & Snieder, R., 2001. Are we exceeding the limits of the great circle approximation in global surface wave tomography?, *Geophys. Res. Lett.,* **28**, 2341–2344.

Spetzler, J., Trampert, J. & Snieder, R., 2002. The effect of scattering in surface wave tomography, *Geophys. J. Int.,* **149**, 755–767.

Tanimoto, T., 2003. Geometrical approach to surface wave finite frequency effects, *Geophys. Res. Lett.,* **30**, 1993, doi:10.1029/2003GL017475.

Tape, C.H., 2003. Waves on a spherical membrane, PhD thesis, Oxford University, Oxford, UK.

Tkalčić, H. & Laske, G., 2002. An evaluation of regionalized models for Eurasia, *EOS, Trans. Am. geophys. Un.,* **83**, F982.

Trefethen, L.N. & Bau, D., III, 1997. *Numerical Linear Algebra, Soc. for Ind. and Appl. Math.*, Philadelphia, PA.

Villaseñor, A., Ritzwoller, M.H., Levshin, A.L., Barmin, M.P., Engdahl, E.R., Spakman, W. & Trampert, J., 2001. Shear velocity structure of Central Eurasia from inversion of surface wave velocities, *Phys. Earth planet. Int.,* **123**, 169–184.

Wang, Z. & Dahlen, F.A., 1995. Spherical-spline parameterization of three-dimensional Earth models, *Geophys. Res. Lett.,* **22**, 3099–3102.

Wang, Z., Dahlen, F.A., Tromp, J. & Ekström, G., 1995. Global and regional structures inferred from surface waves, *EOS, Trans. Am. geophys. Un.,* **76**, 385.

Wang, Z., Tromp, J. & Ekström, G., 1998. Global and local surface-wave inversions: A spherical-spline parameterization, *Geophys. Res. Lett.,* **25**, 207–210.

Wessel, P. & Smith, W.H.F., 1991. Free software helps map and display data, *EOS, Trans. Am. geophys. Un.,* **72**, 445–446.

Widiyantoro, S. & van der Hilst, R.D., 1997. Mantle structure beneath Indonesia inferred from high resolution tomographic imaging, *Geophys. J. Int.,* **130**, 167–182.

Woodhouse, J.H. & Girnius, T.P., 1982. Surface waves and free oscillations in a regionalized earth model, *Geophys. J. R. astr. Soc.,* **68**, 653–673.

Wortel, M.J.R. & Spakman, W., 2000. Subduction and slab detachment in the Mediterranean-Carpathian region, *Science,* **290**, 1910–1917.

Zhou, Y., Dahlen, F.A. & Nolet, G., 2004. 3-D sensitivity kernels for surface wave observables, *Geophys. J. Int.,* submitted.